Journal of Translational Medicine

RESEARCH

Open Access

A single-cell multi-omics atlas defines the cellular and molecular landscape of gastric intestinal metaplasia

Yuman Ye[1,2†], Xiaomin Gong[1†], Sujuan Liu[1], Na Hu[1], Huijie Zhang[1], Xiao Fei[1], Aofei Huang[1], Wentao Fan[1], Zhenping Chen[1], Huan Wang[1], Xingxing He[1], Yi Hu[1], Nonghua Lu[1], Yin Zhu[1], Huajing Ke[1*] and Nianshuang Li[1*]

Abstract

Background Gastric intestinal metaplasia (GIM) is a precancerous lesion closely associated with gastric cancer (GC) risk. A systematic characterization of the molecular profiles across distinct cell types during GIM progression is crucial for devising new intervention strategies and enabling early prevention for GC.

Methods This study integrates single-cell transcriptomics and proteomics data from gastric tissues of patients with mild chronic non-atrophic gastritis (CNAG) and moderate-to-severe GIM.

Results We identified differentially expressed genes (DEGs) and proteins (DEPs) that show consistent changes at both transcriptional and protein levels across epithelial, stromal, and immune cells. Notably, most proteins were downregulated in GIM tissues, potentially linked to reduced expression of RNA splicing-related genes. Epithelial cells in GIM lesions exhibited intestinal-type subpopulations, including goblet and enterocytes, likely originating from gastric isthmus stem cells. Despite overall protein downregulation, the ubiquitin-like protein NEDD8 was markedly upregulated in metaplastic tissues, especially in *H. pylori*-positive tissues. Pathways involved in cytoskeleton maintenance, extracellular matrix stability, and cell adhesion were downregulated, while several macrophage-expressed DEGs/DEPs (e.g., BST2, CYBB, ITGB2) were elevated.

Conclusions This work delineates dynamic transcriptional and translational alterations during the progression from mild gastritis to GIM. It implies that chronic inflammatory injury causes suppress protein synthesis, further driving metaplastic transformation early gastric precancerous lesions.

Keywords Gastric intestinal metaplasia, ScRNA-seq, Proteome, NEDD8

†Yuman Ye and Xiaomin Gong contributed equally to this work.

*Correspondence:
Huajing Ke
ndyfy05069@ncu.edu.cn
Nianshuang Li
ndyfy05390@ncu.edu.cn
[1]Department of Gastroenterology, Jiangxi Provincial Key Laboratory of Digestive Diseases, Jiangxi Clinical Research Center for Gastroenterology, Digestive Disease Hospital, The First Affiliated Hospital, Jiangxi Medical College, Nanchang University, Nanchang, Jiangxi, China
[2]Jiangxi Medical College, Huankui Academy, Nanchang University, Nanchang, Jiangxi, China

Introduction

Gastric cancer (GC) remains a major global public health concern. According to GLOBOCAN 2022 data, GC ranks as the fifth most commonly diagnosis malignancy worldwide and represents the fifth leading cause of cancer-related mortality. The occurrence rate of GC varies geographically, with the highest disease burden observed in East Asia, which accounts for the highest incidence and mortality rates globally [1, 2]. GC is frequently diagnosed at an advanced stage, resulting in poor prognosis [3]. Mounting evidence indicates that gastric carcinogenesis is primarily initiated by *Helicobacter pylori* (*H. pylori*) infection, a well-recognized class I carcinogen, which acts in synergy with environmental and genetic factors to promote oncogenic transformation [4, 5]. Intestinal-type GC, the predominant histological subtype, develops a protracted multi-step process conforming to Correa's cascade, progressing from normal gastric mucosa through chronic non-atrophic gastritis (CNAG), chronic atrophic gastritis (CAG), gastric intestinal metaplasia (GIM), and dysplasia to GC [6]. Thus, a comprehensive understanding of the mechanisms underlying the development of gastric precancerous lesions is crucial for devising novel therapeutic strategies and improving prevention of GC.

A critical step in gastric carcinogenesis is the development of GIM, a premalignant lesion in which the native gastric epithelium is replaced by epithelium resembling that of the small intestine. Patients with IM have a significantly elevated risk of progressing to GC by as much as 6-fold [7, 8]. The initiation of GIM is often triggered by gastric tissue damage caused by *H. pylori* infection, a pathogen that infects nearly 50% of the global population [9]. Accumulating evidence from previous studies and our preliminary data indicates that *H. pylori*-induced gastric epithelium damage and chronic inflammation drive pathological progression through multiple molecular mechanisms. These include immune-inflammatory responses involving activation of innate and adaptive immunity [10, 11], oxidative stress leading to reactive oxygen species (ROS) accumulation and ferroptosis [12], DNA double-strand break (DSB) accumulation resulting in genomic instability [13, 14], and disruption of epithelial integrity that facilitates invasion and migration [15]. Deeper tissue damage further drives the onset of GIM. GIM manifests heterogeneously across patients, encompassing two main histological patterns: complete type I IM, characterized by small intestinal features (absorptive cells, goblet cells, and a brush border); and incomplete type II IM, which displays a colonic-like phenotype [7]. Beyond GIM, another metaplastic subtype, Spasmolytic Polypeptide-Expressing Metaplasia (SPEM), has been widely studied in recent years. SPEM is considered to result from profound injury that causes parietal cell loss, triggering the reprogramming of basal chief cells into metaplastic cells expressing TFF2 or $MUC6^+$/$GSII^+$ markers, or alternatively, it may arise from gastric isthmus progenitor cells [16–18].

To date, only a small number of studies have comprehensively explored the genomic and molecular characteristics of GIM lesions. Our previous work combined single-cell transcriptomics and lipidomics to implicate lipid metabolic reprogramming in GIM pathogenesis, showing elevated triglyceride synthesis and lipid droplet accumulation in gastric tissues with GIM lesions [19, 20]. Huang et al. performed genomic and epigenomic profiling of GIM tissues, revealing recurrent FBXW7 mutations, chromosome 8q amplifications, and telomere shortening [21]. A recent integrative DNA, RNA, and whole exome sequencing data has identified 26 GIM driver genes in diverse pathways including chromatic remodeling (ARID1A) and intestinal homeostasis (SOX9), firmly linking intestinal stem cell to early neoplastic transformation [8]. However, transcriptomic changes often show poor concordance with proteomic alterations, highlighting the need for multi-omics integration to decipher functional molecular events.

In this study, we integrated scRNA-seq and proteomic profiling to analyze human gastric tissues from patients with GIM and those with mild CNAG. GIM is recognized as a critical precancerous lesion sharing transcriptional and protein expression features with some GCs [22, 23], yet the molecular mechanisms driving its progression remain poorly understood. Research indicates that early GC exhibits significant discrepancies between protein expression and transcriptomic levels, highlighting the necessity of a multi-omics approach [24]. Therefore, our study aims to systematically elucidate cellular heterogeneity and differential protein expression patterns across epithelial, stromal, and immune cells, as well as identify key dysregulated pathways in GIM. This comprehensive functional landscape seeks to offer a detailed molecular atlas of GIM progression, ultimately enhancing our understanding and opening new avenues for targeted intervention.

Materials and methods

Human tissue samples

Human gastric tissue samples were collected from patients who underwent endoscopic examination and biopsy at the First Affiliated Hospital of Nanchang University, following the obtainment of written informed consent. The proteomic analysis was performed on tissues from 7 cases of mild CNAG and 7 cases of moderate-to-severe GIM. For immunohistochemistry and immunofluorescence staining, samples from thirty cases per condition were analyzed. All specimens were obtained from the gastric antrum of the patients. This

study was approved by the Ethics Committee of the First Affiliated Hospital of Nanchang University, approval reference number: (2023) CDYFYYLK (01–009). The informed consent was obtained from all participants involved in this study. All procedures were carried out in accordance with the principles of the Declaration of Helsinki. All included cases were recorded in the Human Genetic Resources Center of the First Affiliated Hospital of Nanchang University.

Single-cell RNA-seq data processing

We integrated previously published scRNA-seq data (GSE249874) with publicly available single-cell dataset (GSE134520) retrieved from the Gene Expression Omnibus (GEO) database. The internal sample set contains 6 CNAG and 6 GIM samples, whereas the external sample set contains 3 CNAG and 6 GIM lesions. To remove low-quality cells, a set of criteria was used: (1) Cells were retained if their gene counts and UMI counts fell within the range of the mean ± 2 standard deviations; (2) Cells exhibiting a mitochondrial UMI percentage below 10% were retained; (3) Doublets were removed using DoubletFinder (v2.0.6). Following these three filtering steps, the remaining cells were classified as high-quality cells. Finally, 71,980 cells were obtained for the downstream analysis. We obtained 1553 genes and 5823 UMIs per cell on average. The detailed sequencing data of quality control were shown in Table S1. The FindVariableGenes function from Seurat R package was used to screen highly variable genes (HVGs). To remove the batch effects, harmony (v1.2.3) R package was used. Then the principal component analysis (PCA) was performed based on HVGs, followed by visualization using Uniform Manifold Approximation and Projection (UMAP). To identify cluster-specific marker genes, the FindAllMarkers function from the Seurat package was utilized, which compares the gene expression profile of each cluster with the combined expression profiles of all other clusters. Differential expression analysis was performed using the default parameters (adjusted p-value < 0.05 and |log2 fold change| > 0.25, which can be modified according to actual analysis criteria). The SCP (v0.5.6) R package was used for downstream visualization. To investigate the functional characteristics of distinct cell subtypes compare the differences in biological pathways between the CNAG and GIM groups, Gene ontology (GO), Kyoto Encyclopedia of Genes and Genomes (KEGG) and Gene set Enrichment analysis (GSEA) were performed.

Trajectory analysis

Trajectory inference for epithelial cells was conducted using Monocle3 (v1.4.26). Briefly, the Seurat object containing the epithelial subclusters was converted into a monocle3 object using the as.cell-data-set function from the SeuratWrappers package. The data were normalized and preprocessed using PCA, followed by dimensionality reduction via UMAP. The cells were clustered using the cluster-cells function to ensure the manifold structure was preserved. The root of the trajectory was defined at the node predominantly occupied by isthmus stem cells, selected based on their highest differentiation potential as quantified by CytoTRACE2 (v1.1.0). Pseudotime was calculated relative to this root using the order-cells function. To characterize the gene expression dynamics during differentiation, we utilized the graph-test function to identify genes with spatially variable expression along the trajectory (Moran's I test, q-value < 0.05).

CellChat cell communication analysis

The CellChat (version 1.6.1) R package was used for cell-to-cell ligand–receptor interaction analysis. First, the standardized expression matrix is imported, and CellChat objects are created through the CellChat function. The default parameters were used to identify overexpressed genes, identify overexpressed interactions, and the preprocessing operations project data function. The computeCommunProb, filterCommunication (min. cells = 10) and computeCommun-ProbPathway functions were used to calculate potential ligand–receptor interactions. Finally, the intercellular communication network is aggregated by the aggregateNet function.

Quantitative proteome analysis

Formalin-fixed paraffin-embedded (FFPE) tissue sections (4 μm) from CNAG ($n = 7$) and GIM ($n = 7$) patients were subjected to 4D label-free quantitative proteomic analysis, which was conducted by Shanghai Ouyi Biological Co., Ltd. (Shanghai, China). The clinical characteristics of patients were summarized in Table S2. Briefly, FFPE samples were subjected to deparaffinization and rehydration, followed by antigen retrieval in citrate buffer to reverse protein crosslinks. Proteins were extracted using BT Lysis Buffer supplemented with 1 mM phenylmethylsulfonyl fluoride (PMSF) and protease inhibitors, prior to sonication and centrifugation. The extracted proteins underwent standard reduction, alkylation, and overnight tryptic digestion under continuous agitation. Digested peptides were desalted and quantified via fluorometric assay.

For 4D proteomic analysis, peptides were separated by nanoflow liquid chromatography using a reverse-phase C18 column with an optimized acetonitrile gradient. Before injection, iRT retention time standards were spiked into the samples for chromatographic calibration. MS/MS data were acquired on a timsTOF HT mass spectrometer operating in data-independent diaPASEF mode, which integrates ion mobility separation and

parallel accumulation techniques to improve detection sensitivity.

Raw spectral data were processed using Spectronaut Pulsar 18.7 software with directDIA analysis against the human reference proteome database. Label-free quantification was performed with MaxLFQ normalization across all runs. Proteins not detected in the majority of samples within each experimental group were excluded from subsequent analyses. PCA was performed using the factoextra function in R (v4.5.1) to illustrate the relationships between all variables. The significant differentially expressed proteins (DEPs) were identified based on the criteria Foldchange ≥ 2 or Foldchange ≤ 0.5 with adjusted p-value < 0.05. A heatmap of the top 50 genes was drawn to show the expression of upregulated or downregulated DEPs via the R packet pheatmap. The proteomic profile data in this study have been deposited in ProteomeXchange Consortium (https://proteomecentral.proteomexchange.org) via the iProX partner repository with the dataset identifier PXD071234 [25, 26]. GO and KEGG analyses were performed to analyze the biological processes and signaling pathways, respectively. The GSEA analysis and gene set variation analysis (GSVA) were performed to compare the differences in biological states and pathways between CNAG and GIM. The interactions of up-regulated DEPs were predicted using the STRING website tool (https://string-db.org) with the default parameter [27]. The STRING networks were visualized by Cytoscape (v3.10.3).

ScRNA-seq integrated proteome analysis

Differential gene expression analysis comparing GIM versus CNAG was performed by FindMarkers function within each major cell compartment, including epithelial cells, stromal cells (fibroblasts, endothelial cells, smooth muscle cells), and immune cells (T cells, B cells, macrophages, mast cells). Genes with concordant mRNA-protein expression patterns (co-upregulated or co-downregulated) were identified by conducting Venn diagram analysis between the differentially expressed proteins (DEGs) and previously obtained DEPs from proteomic analysis via VennDiagram (v1.7.3) R package. These overlapping DEGs/DEPs were then visualized through hierarchical clustering heatmaps based on their expression profiles in the proteomic data. Additionally, scaled dot plots of the co-upregulated/co-downregulated genes were generated to identify those specifically expressed in epithelial, stromal, or immune cells, respectively.

Immunohistochemistry

Human gastric tissue specimens were collected from 40 patients with CNAG and 40 patients with GIM at the First Affiliated Hospital of Nanchang University. FFPE tissue Sect. (4 μm) were deparaffinized by incubation in a 70°C oven for 1.5 hours, followed by rehydration through a graded ethanol series. Antigen retrieval was performed by boiling the sections in citrate buffer (pH 6.0) at 95°C for 15 minutes. Endogenous peroxidase activity was blocked with 3% H_2O_2 for 8–10 minutes at room temperature. Sections were incubated overnight at 4°C with primary antibodies. For a full list of primary antibodies used for immunohistochemistry and immunofluorescence, see Table S3. Subsequently, sections were incubated with HRP-conjugated secondary antibody (Dako EnVision+ System) at 37°C for 1 hour. Immunoreactivity was visualized using 3,3'-diaminobenzidine (DAB) chromogen (ZLI-9017, ZSGB-BIO), and sections were counterstained with hematoxylin. Negative controls were processed identically without primary antibodies. All images were acquired using a microscope (Olympus IX 70). Protein expression levels were assessed by trained pathologists and scored based on staining intensity (scale: 0–3) and positive cell frequency (scale: 0–4).

Immunofluorescence

For immunofluorescence analysis, FFPE tissue Sect. (4 μm) from human specimens were deparaffinized and rehydrated as described above. Antigen retrieval was performed by incubating sections in citrate buffer (pH 6.0) at 95 °C for 15 min. Sections were permeabilized with 0.3% Triton X-100 in PBS for 15 min at room temperature, followed by blocking with 3% BSA in PBS for 1 h. Primary antibodies (see Table S3 for details) were applied overnight at 4 °C. After washing with PBS, sections were incubated with Alexa Fluor 488- or 594-conjugated secondary antibodies (1:500 dilution, Invitrogen) in the dark for 1 h at room temperature. Nuclei were counterstained with 4',6-diamidino-2-phenylindole (DAPI). Sections were mounted with DAPI-containing medium and imaged using a fluorescence microscope (Leica Stellaris 5 confocal microscope).

Cell culture, transfection and drug treatment

The human gastric cancer cell line AGS and the immortalized human gastric epithelial cell line HFE145 were cultured in RPMI/1640 and DMEM/F12 medium, respectively. Both media were supplemented with 10% fetal bovine serum (Gibco, Carlsbad, CA) and 1% penicillin/streptomycin (Gibco). All cells were maintained at 37 °C in a humidified incubator with 5% CO_2.

AGS and HFE145 cells were seeded into 6-well plates and allowed to reach 70–80% confluence. Subsequently, they were transfected with siNEDD8 or scrambled control siRNAs (D-Nano Therapeutics, Beijing, China) using the CALNP RNAi reagent in accordance with the manufacturer's instructions. For drug treatment, cells were treated with 0.5 μM MLN4924 (B1036, APExBIO,

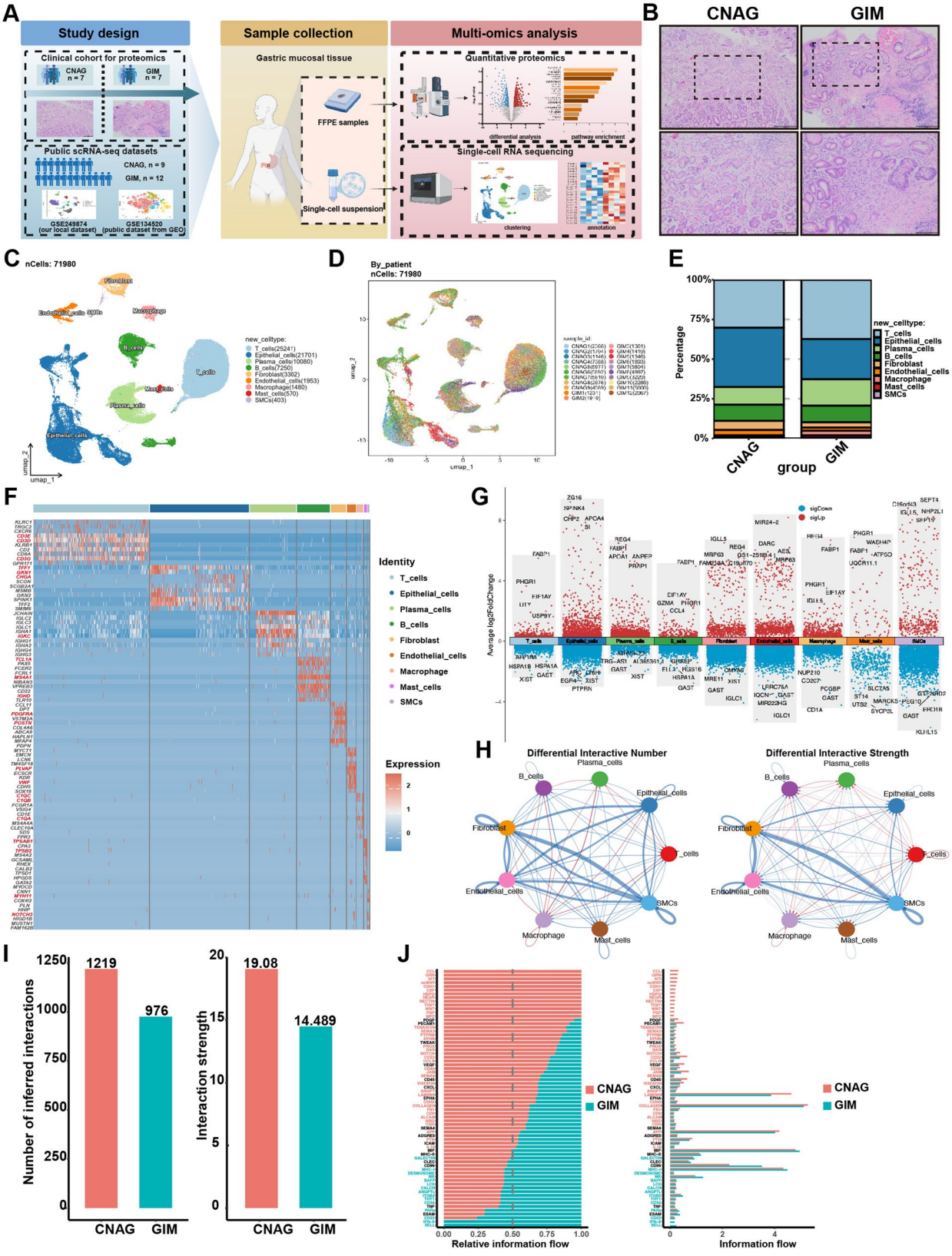

Fig. 1 (See legend on next page.)

(See figure on previous page.)

Fig. 1 A single-cell atlas of human gastric intestinal metaplasia. (**A**) Schematic overview of the single-cell transcriptomic and proteomic profiling of human gastric tissues, including chronic non-atrophic gastritis (CNAG) and gastric intestinal metaplasia (GIM) lesions. (**B**) Representative H&E staining showing the histopathological features of CNAG and GIM tissues. (**C**) UMAP visualization of 71,980 cells, colored by major cell types identified across CNAG and GIM samples. (**D**) UMAP plot of all cells, color-coded by patient of origin to illustrate sample distribution. (**E**) Bar plot depicting the proportional abundance of each cell type from gastric mucosa by stages. (**F**) Heatmap displaying the expression of the top 10 marker genes for each identified cell populations. (**G**) Multiple volcano plots showing DEGs in each cell type when comparing GIM to CNAG tissues. (**H**) Circus plot from CellChat analysis depicting the network of intercellular interaction number and strength. Each color represents a cell type, and edge thickness corresponds to interaction number/strength. (**I**) Bar graph comparing the total number and strength of cellular interactions in CNAG versus GIM tissues. (**J**) Bar plot showing the contribution of signaling networks across CNAG and GIM gastric lesions

Houston, TX, USA) dissolved in DMSO, or an equivalent volume of vehicle control, for 24 h.

H. pylori strain and culture

The rodent-adapted CagA$^+$ *H. pylori* strain pre-murine Sydney Strain 1 (PMSS1) was used in this study. *H. pylori* was streaked onto Brucella agar plates (BD Biosciences, San Jose, CA, USA) containing 5% sheep blood and cultured under microaerophilic conditions at 37 °C. For in vitro co-culture experiments, bacteria were harvested and propagated overnight in Brucella broth (BD Biosciences) supplemented with 10% FBS. Prior to infection, the culture medium of AGS and HFE145 cells was replaced with antibiotic-free medium. Cells were co-cultured with *H. pylori* PMSS1 at various multiplicities of infection (MOI = 0, 25, 50, 100 and 200) for different durations (0 h, 3 h, 6 h, 9 h).

Quantitative reverse-transcriptase PCR (qRT-PCR) analysis

MolPureshang® Flash Cell/Tissue Total RNA kit (YEASEN, Shanghai, China) was used to extract total RNA from cells. For reverse transcription of RNA into cDNA, the FastKing RT Kit (KR116, TIANGEN, Biotech, China) was used. The mRNA levels were quantified using SYBR Green dye and PCR master mix (YEASEN, Shanghai, China) with QuantStudio 5 Real-Time PCR system. The detailed primers information was listed in the Table S4.

EdU assay

Cell proliferation was evaluated using the EdU Cell Proliferation Kit with Alexa Fluor 555 (Shanghai Epizyme Biomedical Technology, Shanghai, China) according to the manufacturer's protocol. Briefly, transfected cells in 6-well plates were incubated with 10 μM EdU solution for 2 h at 37 °C. Following incubation, cells were fixed with 4% paraformaldehyde for 30 min at room temperature, washed three times with PBS, and permeabilized with 0.5% Triton X-100 in PBS for 20 min. the Click-iT reaction cocktail was applied for 30 min to detect EdU incorporation, followed by nuclear counterstaining with DAPI (1 μg/mL) for 10 min. Images were acquired using a Leica SP8 confocal microscope with consistent laser settings across samples. Quantitative analysis was performed by calculating the percentage of EdU-positive cells (red) relative to total DAPI-stained nuclei (blue) in ≥ 5 random fields per condition using ImageJ software.

Western blotting

Whole-cell lysates were prepared using RIPA lysis buffer (R0020, Solarbio, Beijing, China) supplemented with protease and phosphatase inhibitor cocktails (Roche, Amherst, CA, USA), and then the protein concentration was assessed using a BCA assay kit (Thermo Scientific, MA, USA). The cell lysates were separated by 10% SDS-PAGE and transferred onto a nitrocellulose membrane (PerkinElmer, Waltham, MA). After blocking with 5% BSA in PBS, the membranes were incubated overnight at 4 °C with the primary antibodies. Detailed antibody information is listed in the Table S3. After washing three times in TBST, the membranes were incubated with the appropriate horseradish peroxidase (HRP)-conjugated secondary antibodies (Boster, Wuhan, China) for 1 h at room temperature. Immunoreactive bands were detected using enhanced chemiluminescence (ECL) reagents and captured with a Bio-Rad ChemiDoc XRS+ system.

Statistical analysis

All statistical analyses in this study were conducted using GraphPad Prism software or R language. For clinical data analysis, differences in continuous variables between two independent patient groups were assessed using the Mann-Whitney U test. In in vitro experiments, Data were expressed as mean ± standard deviation (SD) of 3 independent experiments. The Wilcoxon rank sum test was used to compare continuous variables between two independent samples. Student's t-test was used to evaluate associations with parametric continuous variables. ****P < 0.001*; ***P < 0.01*; **P < 0.05*.

Results

A single-cell transcriptomic atlas of human gastric intestinal metaplasia, a premalignant lesion

To profile cellular heterogeneity and the associated molecular signatures during the progression of GIM, a precancerous lesion, we performed scRNA-seq and proteomic analyses. For transcriptomic characterization at single-cell resolution, we integrated scRNA-seq data from our previously published cohort (GSE249874) with a publicly available dataset (GSE134520) contributed by

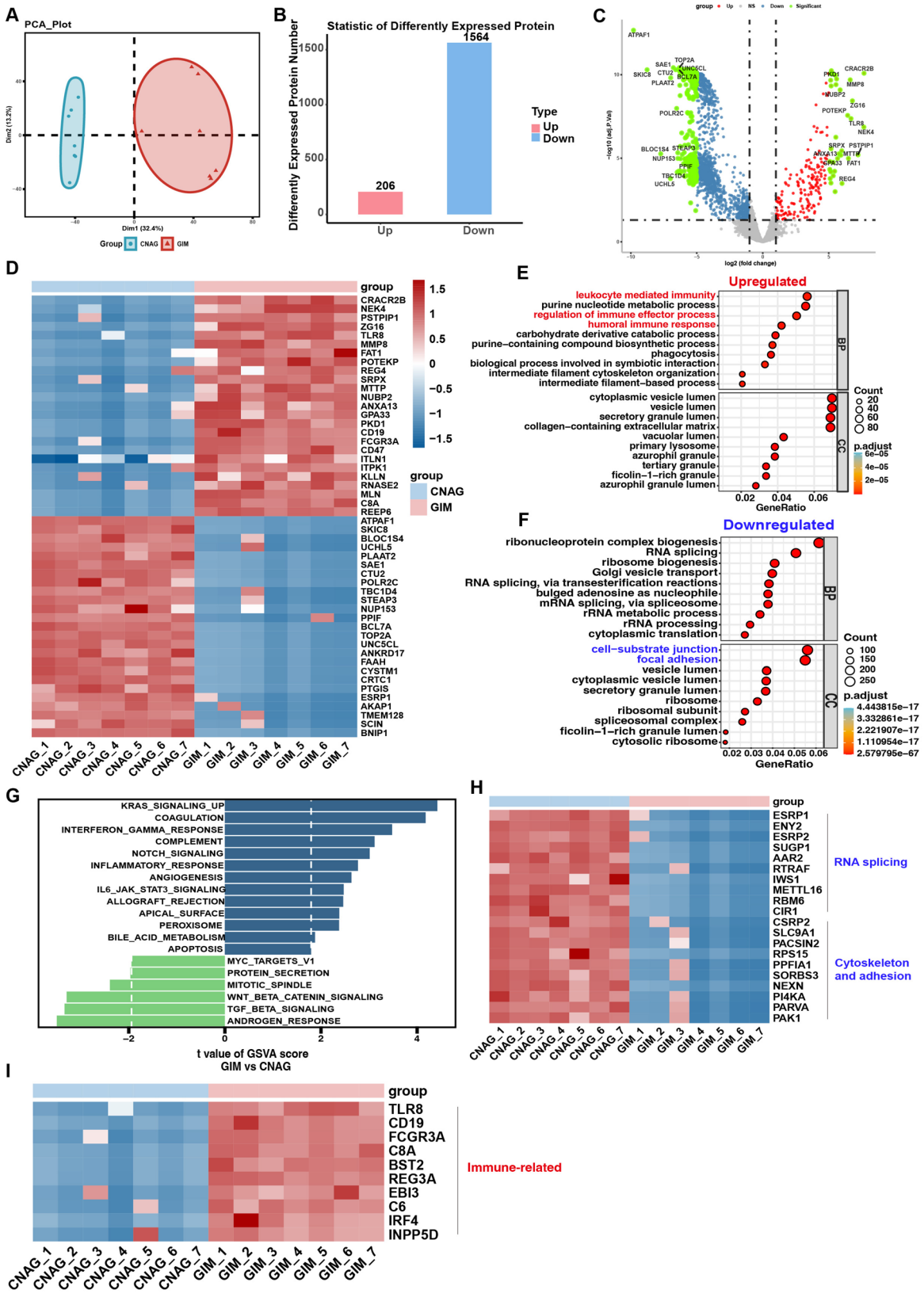

Fig. 2 (See legend on next page.)

(See figure on previous page.)

Fig. 2 The proteomic landscape of GIM progression reveals differential protein expression and altered pathways. (**A**) PCA of the proteomic data, indicating variance between and within groups. (**B**, **C**) Bar plot (**B**) and volcano plot (**C**) of proteins differentially expressed in GIM compared to CNAG (|log2FC|>1, *P*<0.05). (**D**) Heatmap displaying the top 25 significantly upregulated and downregulated proteins in GIM lesions compared to CNAG tissues. (**E**, **F**) GO enrichment analysis of biological processes and cellular components for the significantly upregulated (**E**) and downregulated (**F**) proteins. (**G**) GSVA revealing pathways that are significantly activated or suppressed in GIM lesions compared to CNAG tissues. (**H**) Heatmap showing significantly downregulated proteins related to RNA splicing and cell adhesion; (**I**) Heatmap illustrating significantly upregulated proteins related to immune responses in GIM lesions compared to CNAG

a colleague of Professor Shao Li. This combined dataset comprised a total of 9 CNAG and 12 GIM specimens. To complement this with deep proteomic coverage, we performed 4D-label-based quantitative proteomics on FFPE tissue sections from a separate set of CNAG and GIM samples (Fig. 1A). As shown in Fig. 1B, representative pathological features of CNAG and GIM were presented. We analyzed a total of 71,980 cells after quality control and batch effect correction. Cell clusters were annotated based on established lineage-specific markers: epithelial cells (*EPCAM*, *KRT19*); T cells (*CD3D*, *CD3G*); endothelial cells (*PECAM1*, *CDH5*); B cells (*CD79A*); macrophages (*CD68*, *CSF1R*); fibroblasts (*COL1A1*, *PDGFRA*); mast cells (*TPSAB1*, *TPSB2*); smooth muscle cells (*SMCs*; *TAGLN*, *ACTAT2*); and plasma cells (*IGKC*, *MZB1*) (Fig. 1C and Fig. S1A, B). The top20 marker genes for each cell type were presented in Table S5. Analysis revealed a profound heterogeneity and patient-specific expression pattern within the epithelial compartment (Fig. 1D). Notably, the proportion of epithelial cells was significantly decreased in GIM relative to CNAG, suggesting a potential disruption of the epithelial cells. In contrast, macrophages, pivotal to chronic inflammation, were more abundant in GIM (Fig. 1E and Fig. S1C). A heatmap summarizing the top 10 marker genes for each of the identified cell types (Fig. 1F). We next identified significantly DEGs in each major cell type between CNAG and GIM lesions (Fig. 1G). To investigate changes in cell-cell communication within the gastric microenvironment during GIM progression, we applied CellChat analysis. Notably, GIM lesions exhibited a remarkable reduction in both the number and strength of cell-cell interactions compared to CNAG (Fig. 1H, I and Fig. S1D, E). Analysis of the signaling networks revealed that certain pathways such as TIGIT, CDH1 and GRN, were more active in CNAG, while others such as SELL and IFN-II were predominant in precancerous GIM lesion (Fig. 1J).

Proteomic profiling reveals dysregulated proteins and altered pathways activity in human gastric intestinal metaplasia

Given the frequent discordance between transcriptomic and proteomic expression, we performed proteomic profiling of human gastric tissues from mild CNAG and moderate-to-severe GIM to characterize molecular alterations underlying GIM development. The proteome of the two groups were clearly distinguishable by PCA (Fig. 2A). Applying thresholds of $|\log_2 FC|>1$ and adjust P value<0.05, we identified 1,770 DEPs. Strikingly, the proteomic landscape in GIM was predominantly downregulated, with 1,564 proteins decreased and only 206 increased (Fig. 2B, C). The top 25 significantly upregulated and downregulated proteins in GIM versus CNAG specimens were displayed in Fig. 2D. GO enrichment analysis indicated that upregulated proteins in GIM were predominantly linked to immune response regulation, whereas downregulated proteins were involved in RNA splicing, ribosome biogenesis, cell-cell junction and focal adhesion processes (Fig. 2E, F). GSVA confirmed elevated activity in immune-inflammatory pathways such as IFNγ response, complement and STAT3 signaling in GIM lesion, but reduced activity in protein secretion and androgen response pathways (Fig. 2G). The regulators of RNA splicing, including ESRP1, ENY2, and METTL16, along with proteins involved in cellular cytoskeletal and adhesion, such as PAK1 and PARVA, were significantly downregulated in GIM compared to CNAG (Fig. 2H). In contrast, immune-related proteins like TLR8, CD19, and IRF4 were markedly upregulated in GIM lesion (Fig. 2I). In summary, our findings define the proteomic remodeling and functional reprogramming that underlies the progression of GIM.

PPI network analysis implicates ITGB2 and CYBB as potential drivers of intestinal metaplasia

To identify central regulators involved in GIM progression, we performed a PPI network analysis of the significantly altered proteome. As a result, this approach nominated ITGB2, LTF, CYBB, MMP9 and CTSG as core nodes in the network (Fig. 3A). The cell type-specific expression patterns of these proteins, derived from single-cell RNA sequencing, are shown in Fig. 3B. This transcriptional upregulation was confirmed at protein level by proteomic analysis (Fig. 3C). Given the low baseline mRNA levels of *LTF*, *MMP9* and *CTSG* (Fig. S2A-C), we focused on *ITGB2*, an integrin subunit governing immune cell adhesion and migration, and *CYBB*, a core component of the NADPH oxidase complex. Transcript levels of both genes were significantly elevated in GIM compared to CNAG and were predominantly localized to immune cells (Fig. 3D, E). This finding was further supported by IHC analysis, which showed markedly increased ITGB2 and CYBB expression in human GIM

specimens (Fig. 3F-I). Collectively, these data suggest that upregulation of ITGB2 and CYBB may contributes to GIM progression by orchestrating immune cell infiltration and perpetuating chronic inflammation.

Gastric epithelial reprogramming and intestinal cell lineage expansion in gastric intestinal metaplasia

We next profiled gastric epithelial subpopulations by analyzing 21,640 cells, which were clustered via UMAP into 15 distinct groups (Fig. S3A). Based on established marker genes, we annotated 13 epithelial cell types: surface mucous cells (*TFF1*, *MUC5AC*), G cells (*GAST*), goblet cells (*MUC2*, *SPINK4*, *OLFM4*), neck mucus cells (*MUC6*), differentiated epithelial cells (*LSAMP*), isthmus stem cells (*TOP2A*, *CDK1*, *MKI67*), stressed epithelial cells (*HSPA1B*, *HSPA6*), X cells (*GHRL*), neuroendocrine cells (*CARTPT*), enterocytes (*FABP1*, *APOA4*), D cells (*SST*), immune-reactive epithelial cells (*HLA-DRB1*, *HLA-DPA1*), and enteroendocrine cells (*CHGA*, *CHGB*) (Fig. 4A, B). Notably, both CNAG and GIM samples exhibited substantial epithelial heterogeneity and distinct molecular signatures (Fig. 4C and Fig. S3B). Specifically, we observed a marked expansion of intestinal lineages, including enterocytes and goblet cells, in GIM lesions, accompanied by a corresponding decrease in gastric lineages such as surface mucous cells and G cells (Fig. 4D). To trace the origin of the expanded intestinal lineages in GIM, we performed trajectory inference using Monocle3. This analysis suggested that both enterocytes and goblet cells may originate from isthmus stem cells (Fig. 4E and Fig. S3C). This finding aligns with a recent single-cell transcriptomics study revealing a similar origin for GIM lesions in patient-derived organoids [28]. These cell lineages were molecularly defined by the specific high expression of APOA4 and OLFM4, respectively (Fig. S3D). Moreover, immunofluorescence analysis confirmed the expansion of $EPCAM^{+}OLFM4^{+}$ and $EPCAM^{+}APOA4^{+}$ intestinal epithelial subpopulations in GIM tissues (Fig. 4F, G). Consistently, immunohistochemistry staining indicated markedly increased expression of both OLFM4 and APOA4 expression in GIM lesions compared to CNAG controls (Fig. 4H, I). Additionally, GSEA of GO terms on epithelial cells revealed significant pathways alterations in GIM versus CNAG. In line with our proteomic findings, immune-related pathways such as antigen presentation, whereas biosynthetic processes including RNA biosynthetic process were downregulated (Fig. 4J).

NEDD8 upregulation drives *H. pylori*-induced gastric inflammation and metaplastic transition

We employed a multi-omic approach to delineate the altered molecular landscape in GIM. By cross-referencing single-cell transcriptomic data from epithelial cells with bulk proteomic data, both comparing GIM to CNAG, we identified 23 concordantly upregulated and 376 concordantly downregulated genes/proteins in GIM (Fig. 5A). Expression patterns of the 23 upregulated DEGs/DEPs across individual samples were displayed in Fig. 5B, while the top 25 downregulated candidates were shown in Fig. 5C. We then focused on epithelial cell-specific genes within this concordant set. Notably, key epithelial genes, such as CLDN18, MUC1, VSIG2 and SDC4, were significantly downregulated in GIM lesion at both transcriptional and protein levels (Fig. S4A). Beyond the expected upregulation of established markers FABP1, MUC13 and TFF3 (Fig. 5B), our multi-omics screen intriguingly identified NEDD8, a ubiquitin-like protein that regulates protein stability via neddylation [29], as a novel candidate upregulated in GIM compared to CNAG at both mRNA and protein levels (Fig. S4B). Consistent with our omics data, NEDD8 primarily localized to the nucleus, was significantly more abundant in human GIM tissues than in CNAG samples (Fig. 5D, E). Notably, among CNAG samples, *H. pylori*-positive cases exhibited higher NEDD8 levels than *H. pylori*-negative ones (Fig. 5D, F). Functionally, differential GO analysis between epithelial cells stratified into NEDD8-high (top 25%) and NEDD8-low (bottom 25%) groups revealed that NEDD8 was significantly associated with ubiquitin-like protein transferase activity and transcriptional co-regulation (Fig. 5G). To validate these functional associations and determine whether NEDD8 actively mediates *H. pylori* infection dynamics, we established an in vitro infection model in gastric epithelial cells. Immunoblotting revealed that *H. pylori* infection increased the protein levels of NEDD8 in HFE145 cells with a trend in a MOI-dependent manner, however, this increase was not time-dependent (Fig. 5H, I). Given that key proteins such as IκBα and P53 are established neddylation substrates [30, 31], we evaluated the role of NEDD8 in *H. pylori*-induced signal transduction. Pretreatment with the NEDD8-activating enzyme inhibitor MLN4924 prior to infection significantly accumulated P53, IκBα, and p-IκBα proteins, while concurrently reducing p-P65 levels (Fig. 5J, L), indicating that NEDD8 facilitates *H. pylori*-induced NF-κB activation. Furthermore, MLN4924 treatment profoundly attenuated the *H. pylori*-driven upregulation of the chemokine CXCL1 and pro-inflammatory cytokines IL-1β, IL-6, and IL-8 (Fig. 5K, M). Consistently, targeted silencing of NEDD8 via siRNA yielded similar suppressive effects on these inflammatory mediators (Fig. S4C-F). Notably, EdU incorporation assays showed that MLN4924 effectively reversed the *H. pylori*-driven hyperproliferation of gastric epithelial cells (Fig. 5N, O), linking NEDD8 to the *H. pylori*-mediated suppression of P53 and the aberrant proliferative phenotype. Taken together, these findings suggest that *H. pylori* infection upregulates NEDD8

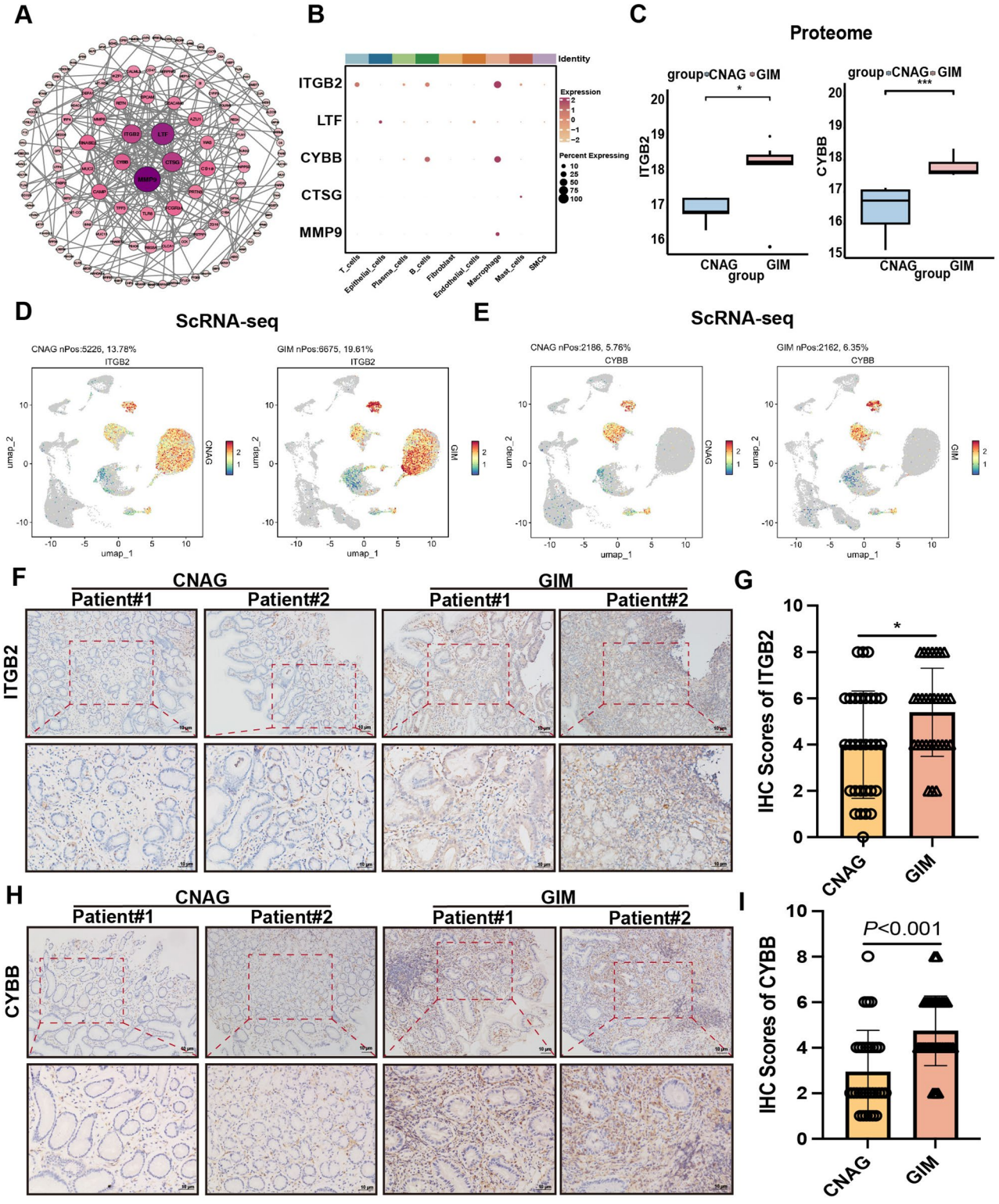

Fig. 3 PPI network analysis implicates ITGB2 and CYBB as potential mediators during the progression of intestinal metaplasia. (**A**) PPI network identifying differentially expressed proteins occupying central regulatory hubs. (**B**) Dot plot illustrating the cell type-specific expression distribution of core DEPs, such as ITGB2, LTF, CYBB, CTSG and MMP9) derived from scRNA-seq data. (**C**) Box plots comparing the abundance of ITGB2 and CYBB proteins in human gastric tissues from CNAG and GIM cohorts, as quantified by proteomic analysis. (**D**, **E**) UMAP projections visualizing the expression patterns of ITGB2 (**D**) and CYBB (**E**) across the cellular landscape. (**F**) Representative IHC images showing ITGB2 expression in human CNAG and GIM tissues. Scale bar, 10 μm. (**G**) Quantification of ITGB2 IHC staining intensity across CNAG and GIM samples. (**H**) Representative IHC images illustrating CYBB protein expression in human CNAG and GIM tissues. Scale bar, 10 μm. (**I**) Quantification of CYBB IHC staining intensity across CNAG and GIM samples. **P<0.05*, ***P<0.01*, ****P<0.001*

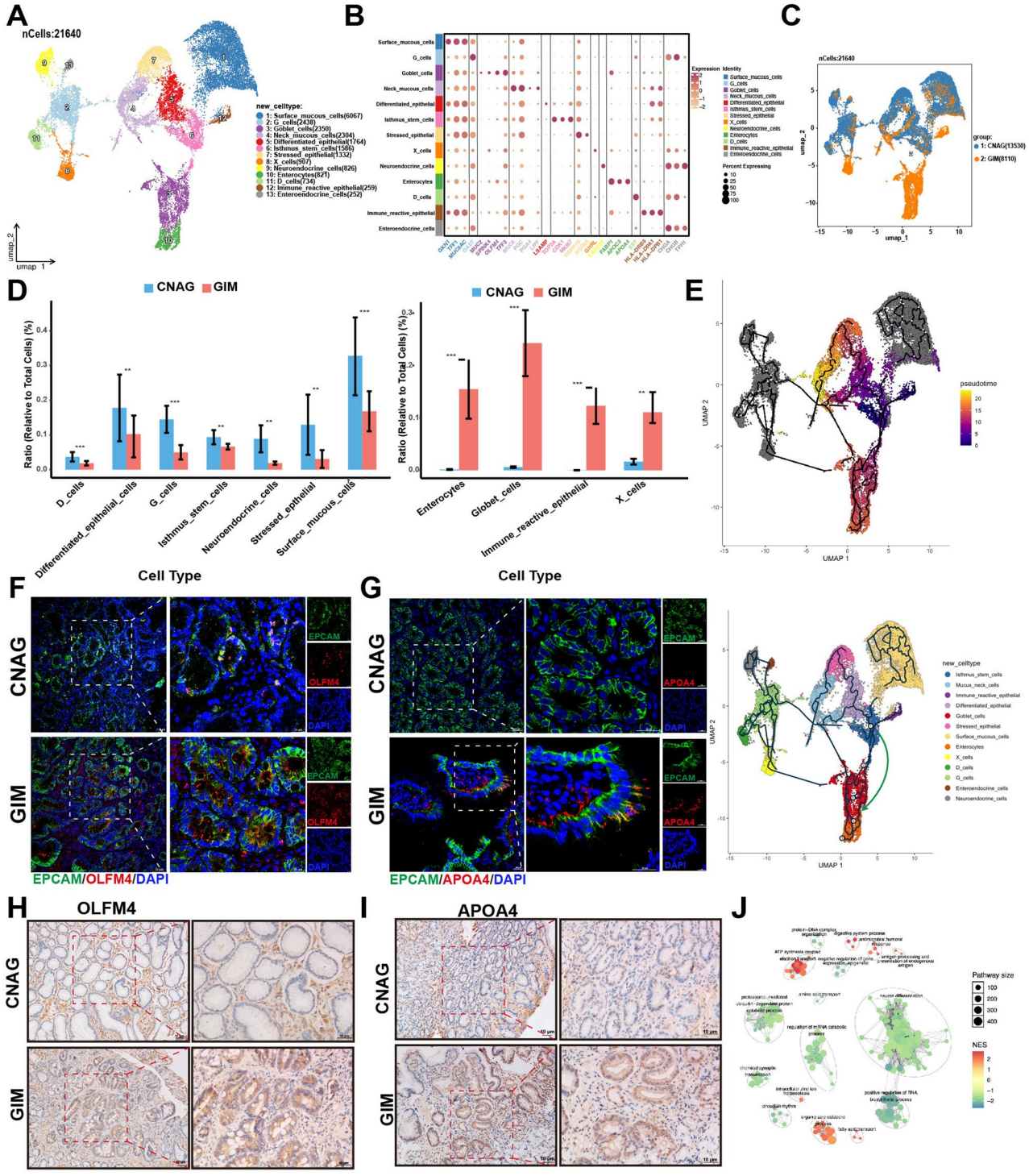

Fig. 4 Distinct epithelial cells subclusters between CNAG and GIM. (**A**) UMAP visualization of the epithelial cell subclusters. (**B**) Dot plot displaying the expression of marker genes of each epithelial subtypes. (**C**) UMAP plot of epithelial cell subtypes, color-coded by the histopathological condition, CNAG or GIM. (**D**) Proportional abundance of each epithelial subcluster in tissues from CNAG and GIM patients. (**E**) Pseudotemporal trajectory analysis using Monocle 3, inferring the cell origin and branching path of differentiation into enterocyte and goblet cells, which were highly abundant in GIM. (**F**, **G**) Representative immunofluorescence images of gastric tissues from CNAG and GIM, showing $EPCAM^+OLFM4^+$ cells (**F**), and $EPCAM^+APOA4^+$cells. (**G**) Nuclei are counterstained with DAPI. Scale bar, 20 μm. (**H**, **I**) Representative IHC images and quantitative staining scores for OLFM4 (**H**) and APOA4 (**I**) in CNAG and GIM gastric tissues. Scale bar, 10 μm. (**J**) GSEA of the GO gene sets on epithelial cells, comparing GIM to CNAG. The heatmap displays NES value, with red and green indicating upregulated and downregulated pathways, respectively. **P<0.05*, ***P<0.01*, ****P<0.001*

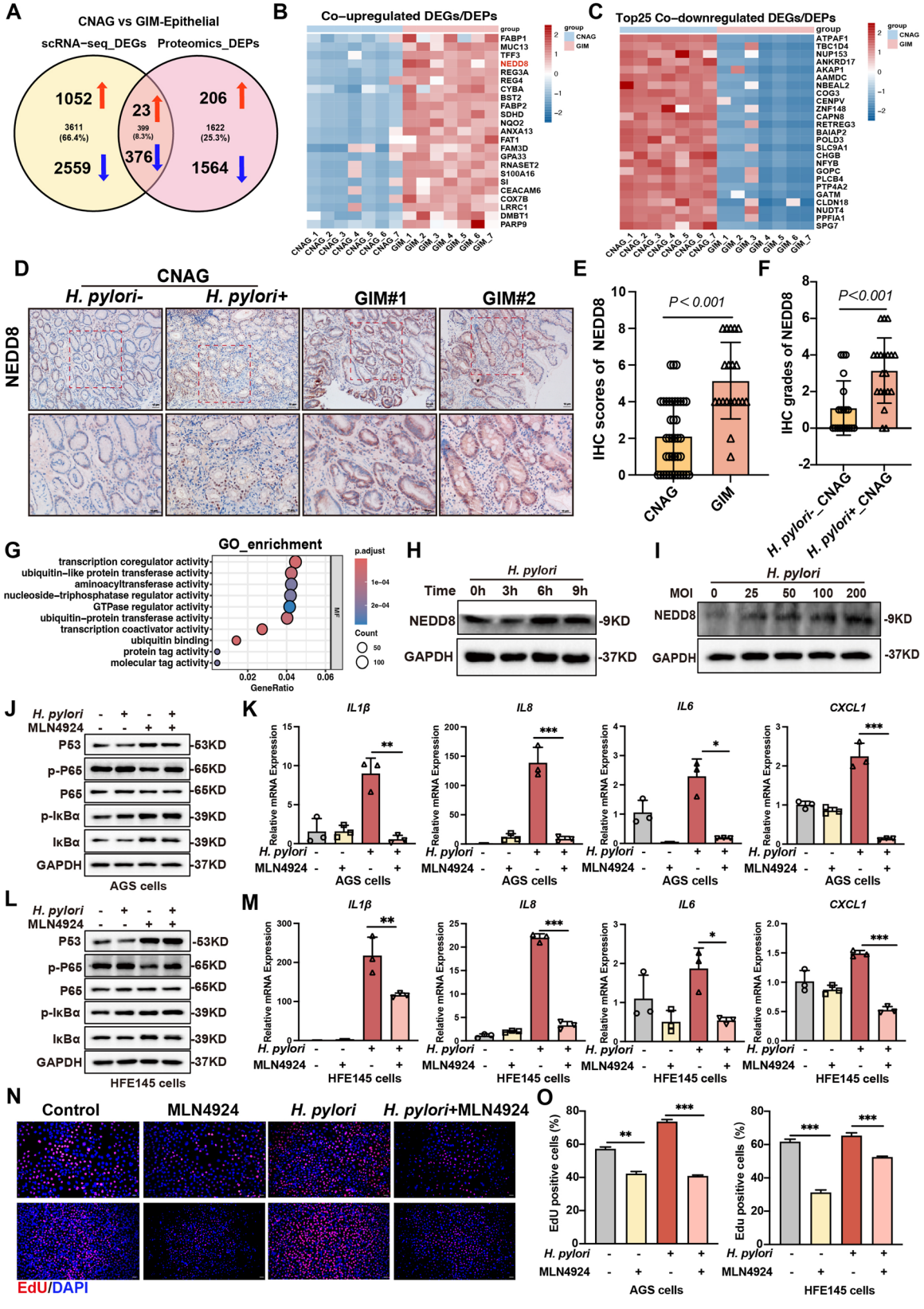

Fig. 5 (See legend on next page.)

(See figure on previous page.)

Fig. 5 NEDD8 upregulation drives *H. pylori*-induced gastric inflammation and metaplastic transition. **(A)** Venn diagram illustrating the overlap between epithelial DEGs from scRNA-seq and DEPs from proteomics in the comparison of CNAG versus GIM. (**B**) Heatmap showing the 23 commonly upregulated DEGs /DEPs. (**C**) Heatmap displaying the Top 25 commonly downregulated DEGs/DEPs. (**D**) Representative IHC images of NEDD8 expression in *H. pylori*-positive and -negative CNAG and GIM tissues. Scale bar, 10 μm. (**E**, **F**) Statistical comparison of IHC scores for NEDD8 expression between CNAG and GIM tissues (**E**), as well as between *H. pylori*-positive and -negative CNAG tissues (**F**). (**G**) GO enrichment analysis identifying biological functions regulated by NEDD8. (**H**, **I**) Western blot assay for NEDD8 protein expression in HFE145 cells treated with *H. pylori* at an MOI of 100 for indicated time points (**H**), or infected with *H. pylori* at various MOIs for 24 h (**I**). (**J**, **L**) AGS (**J**) and HFE145 (**L**) cells were treated with MLN4924 and *H. pylori* as indicated. Western blotting was performed to detect the proteins of P53 and NF-κB pathways, including p-P65, P65, p-IκBα and IκBα. (**K**, **M**) Expression levels of CXCL1, IL-1β, IL-6, and IL-8 in AGS (**K**) and HFE145 (**M**) cells were measured by qRT-PCR across the four indicated groups. (**N**) EdU incorporation assay was performed to assess the proliferation of AGS and HFE145 cells. (**O**) The percentage of EdU-positive cells was quantified. Scale bar, 10 μm. **P<0.05*, ***P<0.01*, ****P<0.001*

expression to drive NF-κB activation, inflammatory cytokine production, and aberrant epithelial proliferation. This cascade likely serves as an early driver of GIM lesion development.

Stromal remodeling accompanied by a distinct molecular profile in GIM progression

We identified 5,658 stromal cells, which were categorized into five fibroblast subsets (Fibro_C1-C5), three endothelial cell subsets (Endo_C1-C3), pericytes, and SMCs (Fig. 6A and 9A). These stromal cell subtypes exhibited distinct heterogeneity between CNAG and GIM tissues (Fig. 6B). Specifically, the Fibro_C1 and Fibro_C2 subsets were significantly diminished in GIM, whereas the Fibro_C4 subset was notably expanded (Fig. 6C). Functional characterization revealed the Fibro_C1 cells, expressing high levels of RBP4 and CPM, were enriched in biological processes such as focal adhesion. Fibro_C2 cells, marked by FBN2 and NRG1 expression, were associated with ECM-receptor interaction and the cytoskeleton in muscle cells (Fig. 6D, E). In contrast, the GIM-enriched Fibro_C4 subset, marked by FAM105A and MGST1, showed upregulation in pathways such as ROS, proteasome, and oxidative phosphorylation, but downregulation in adherens junction and focal adhesion pathways upon KEGG analysis (Fig. 6D, F). GSEA analysis of GO terms indicated a marked downregulation in histone modifying activity and double-strand break repair pathways in stromal cells of GIM lesions compared to CNAG (Fig. 6G).

An integrated analysis of stromal cell transcriptomics and bulk tissue proteomics defined a core signature of 18 upregulated and 321 downregulated DEGs/DEPs in GIM (Fig. 6H). This signature included key stromal-specific genes that were consistently downregulated at both molecular levels. Notably, fibroblast-expressed genes (e.g., POSTN, MXRA5, COL5A2, PRKG1) and endothelial-expressed genes (e.g., CD93, CD36, CAVIN2) were prominently suppressed in GIM lesions (Fig. 6I, J).

Immune cell-associated differential protein profiles in GIM revealed by integrated scRNA-seq and proteomics

Unsupervised clustering of 32,114 immune cells identified 11 major cell types (Fig. 7A). These included three CD8$^+$T cell subsets (GZMK$^+$IL7R$^+$, XCL2$^+$HOPX$^+$, and TOX2$^+$CTLA4$^+$), an IL17A$^+$CCL20$^+$ CD4$^+$ T cell subset, natural killer T (NKT) cells, three B cell subsets (IGHD$^+$VPREB3$^+$, MKI67$^+$TOP2A$^+$, and LMO2$^+$MEF2B$^+$), plasma cells, macrophages, and mast cells. Comparative analysis revealed that macrophages were significantly more abundant in human GIM tissues, whereas the TOX2$^+$CTLA4$^+$CD8$^+$T cell subset was notably reduced (Fig. 7B). The top five marker genes for each immune cell subset are displayed in Fig. 7C. To pinpoint key immune-related molecular changes in gastric intestinal metaplasia (GIM), we cross-referenced differential genes from immune cell single-cell transcriptomics with differential proteins from bulk proteomics. This integrated analysis identified a striking imbalance in gene/protein expression in GIM versus CNAG, with only 6 concordantly upregulated but 99 downregulated DEGs/DEPs (Fig. 7D). Notably, 5 of the 6 upregulated immune cell-associated genes that were upregulated in GIM lesions were predominantly expressed in macrophages, including BST2, SDHD, CYBA, MGST3, and ITGB2 (Fig. 7E). Correspondingly, the protein levels of these markers were significantly increased in GIM lesions compared to CNAG (Fig. 7F). Conversely, the extensively downregulated immune-related DEGs/DEPs were enriched in processes like RNA splicing and chromosomal structure (Fig. S4B). Together, these data point to a pivotal role for macrophage infiltration and the associated molecular reprogramming in propelling the transition from inflammatory chronic gastritis to metaplastic lesions.

Discussion

GIM is an important precancerous condition for GC. However, clinical management relies primarily on endoscopic surveillance due to a lack of effective pharmacological interventions, as the molecular basis of its progression remains poorly understood [7, 32]. Often, transcript levels fail to correlate reliably with corresponding protein abundance [24]. In this study, we constructed a comprehensive atlas of the cellular and molecular dynamics during GIM progression by integrating scRNA-seq with proteomic profiling. Notably, we found that the majority of proteins were downregulated in metaplastic tissues, accompanied by the suppression of RNA

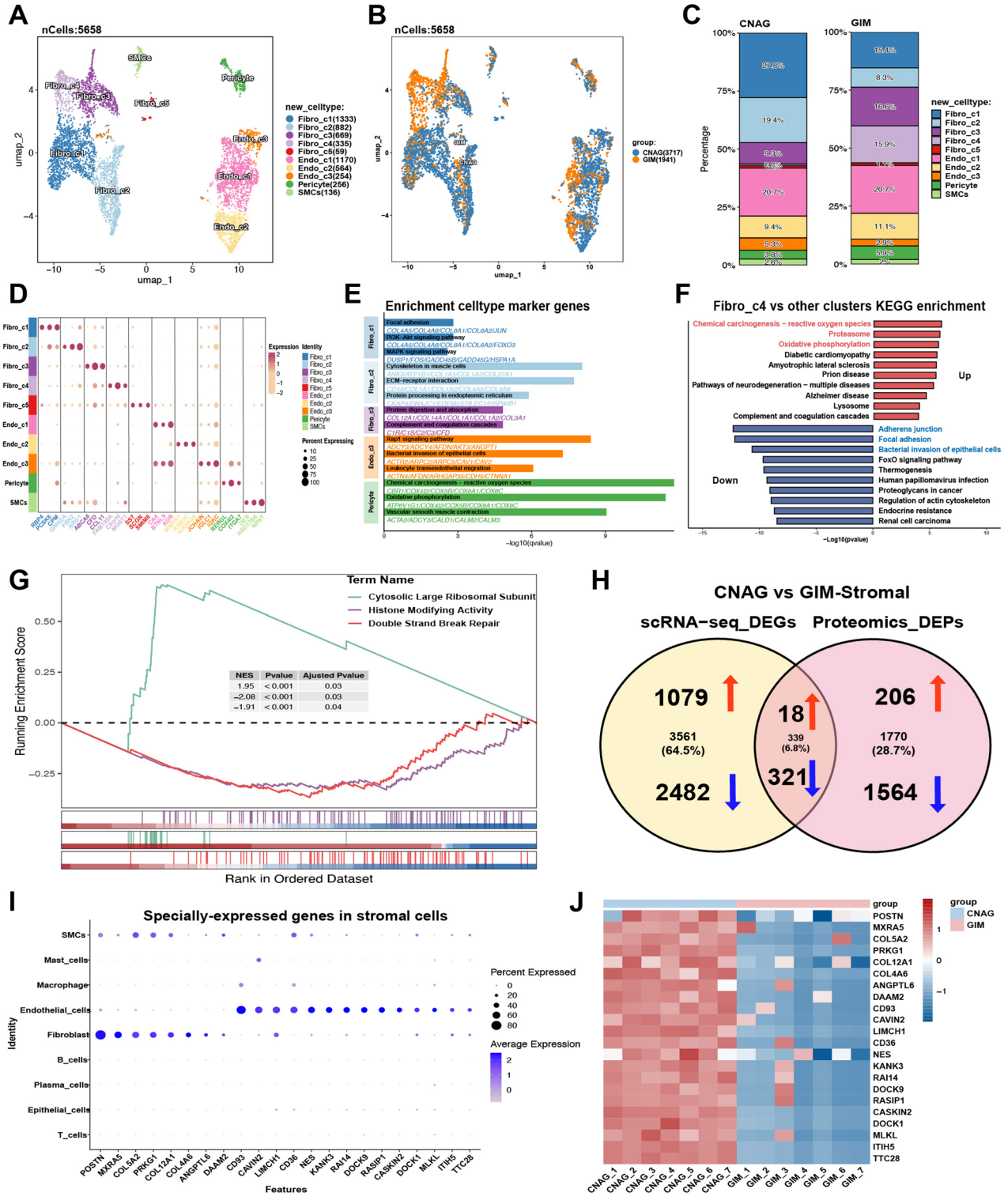

Fig. 6 (See legend on next page.)

splicing-related biological processes. Despite the overall reduction, the ubiquitin-like protein NEDD8, along with ITGB2 and CYBB that highly expressed in macrophages, were significantly upregulated in GIM. Furthermore, we identified and profiled a set of genes that exhibited concordant changes at both transcriptional and protein levels across epithelial, stromal, and immune cells in metaplastic tissues. Our analysis revealed that GIM stage

(See figure on previous page.)

Fig. 6 Stromal cell heterogeneity and specific protein profiles in intestinal metaplasia lesion revealed by integrated scRNA-seq and proteomics. (**A**) UMAP visualization of 5658 stromal cells, categorized intro fibroblast, endothelial, and smooth muscle cell subpopulations. (**B**) UMAP plot colored by tissue diagnosis, depicting the distribution of stromal cell subpopulations across CNAG and GIM stages. (**C**) Bar plot quantifying the proportion of each defined stromal cell subtypes. (**D**) Dot plot displaying the expression of top 3 marker genes for each stromal cell subtype. (**E**) KEGG pathway enrichment analysis identifying key biological pathways for the indicated stromal subclusters. The top enriched pathways were shown, with the corresponding highly expressed genes listed below. (**F**) KEGG functional enrichment analysis for the Fibro_C4 subcluster, which was significantly expanded in GIM. (**G**) GSEA of stromal cells comparing GIM to CNAG tissues, displaying significantly upregulated and downregulated pathways. (**H**) Venn diagram identifying the overlapping DEGs/DEPs in GIM compared to CNAG, derived from both scRNA-seq and proteomic data. (**I**) Dot plot featuring the commonly downregulated DEGs/DEPs that were specifically expressed in stromal cells. (**J**) Heatmap depicting the expression patterns of stromal-specific, commonly downregulated DEPs in GIM versus CNAG lesions

was characterized by diminished gastric lineages and expanded intestinal lineages, a proliferative Fibro_c4 subset propagating oxidative stress responses and defective cytotoxic immunity. Taken together, these findings pave the way for new therapeutic interventions and improve risk stratification in early gastric precancerous lesions.

While previous studies have extensively characterized the genomic and transcriptomic landscapes of GC [33, 34], the molecular dynamics underlying the premalignant transition to GIM remain less defined. A key finding of our multi-omics integration is the marked uncoupling between transcriptomic and proteomic signatures during the metaplastic transition. Specifically, we observed a profound downregulation of RNA splicing machinery, cytoskeleton maintenance, and cell adhesion networks within the metaplastic epithelium. This suggests that the reprogramming of gastric cells into an intestinal phenotype requires a fundamental destabilization of normal epithelial architecture and synthetic machinery. Against this backdrop of structural and synthetic suppression, the *H. pylori*-associated upregulation of NEDD8 presents a notable biological exception. Importantly, our in vitro model suggest that *H. pylori* infection upregulates NEDD8 expression, which promotes NF-κB activation, the secretion of pro-inflammatory cytokines, and aberrant epithelial proliferation. These findings of our study move beyond technical profiling to provide a novel biological framework for GIM pathogenesis, serving as a foundational reference for future mechanistic investigations and targeted interception.

Our proteomic analysis revealed widespread protein downregulation in GIM lesion, with approximately 88% of DEPs showing reduced abundance. Concurrently, pathways critically involved in protein synthesis, including RNA splicing and translation, were significantly suppressed. These findings align with established stress response mechanisms wherein cells activate integrated stress response (ISR) network through pathways such as eukaryotic initiation factor 2α (eIF2α) phosphorylation to globally suppress translation during hypoxia, viral infection, or other environmental challenges [35]. Given that GIM is commonly regarded as a gastric chronic inflammation-driven lesion, we propose that the observed inhibition of spliceosomal activity, ribosome biogenesis and Golgi vesicle transport is likely to serve as an adaptive survival strategy by reducing metabolic load and preventing misfolded protein accumulation through translational suppression [36]. Our findings were further supported by the process of paligenosis, wherein mature cells downregulate mTOR activity and metabolic programs to enable dedifferentiation and repair [37]. Furthermore, stress-induced alternative splicing emerges as a critical regulatory mechanism, consistent with documented responses to heat shock, ER stress, and viral infections, where selective generation of splice variants enables dynamic proteome remodeling and precise modulation of stress-responsive gene networks [38, 39]. Our data provide a novel framework for understanding how gastric cells initiate protective response against persistent inflammation, which are subsequently co-opted, ultimately leading to the advancement of metaplastic lesions.

Complementary to proteomic analysis, single-cell approaches are providing important insights into the lineage heterogeneities of metaplastic cells [8]. During gastric carcinogenesis, epithelial cells undergo dynamic phenotypic alterations transitioning from normal gastric epithelium to an intestinal-like phenotype in response to chronic injury, which can progress through metaplasia to invasive adenocarcinoma via genetic and epigenetic alterations and interactions with the stromal microenvironment [40, 41]. In this study, we observed the expansion of intestinal lineage, including goblet cells and enterocytes, during intestinal metaplasia condition, consistent with prior reports [8, 42]. Notably, our findings extend this knowledge by pointing to potential origin in isthmus stem cells. This notion is supported by a recent organoid study, which identified STMN1 cycling isthmus stem cells as the origin of IM, with a heightened potential for malignant transformation [28]. A technical note is that the stem cell marker OLFM4 was difficult to resolve from goblet cells in our dataset, possibly due to low stem cell abundance. OLFM4 as a potential marker of incomplete intestinal metaplasia and demonstrated its role in driving the malignant progression of gastric precancerous lesions through activation of the MYH9/GSK3β/β-catenin pathway [43]. Moreover, integrated proteomic analysis revealed that proteins downregulated in gastric epithelial cells were primarily associated

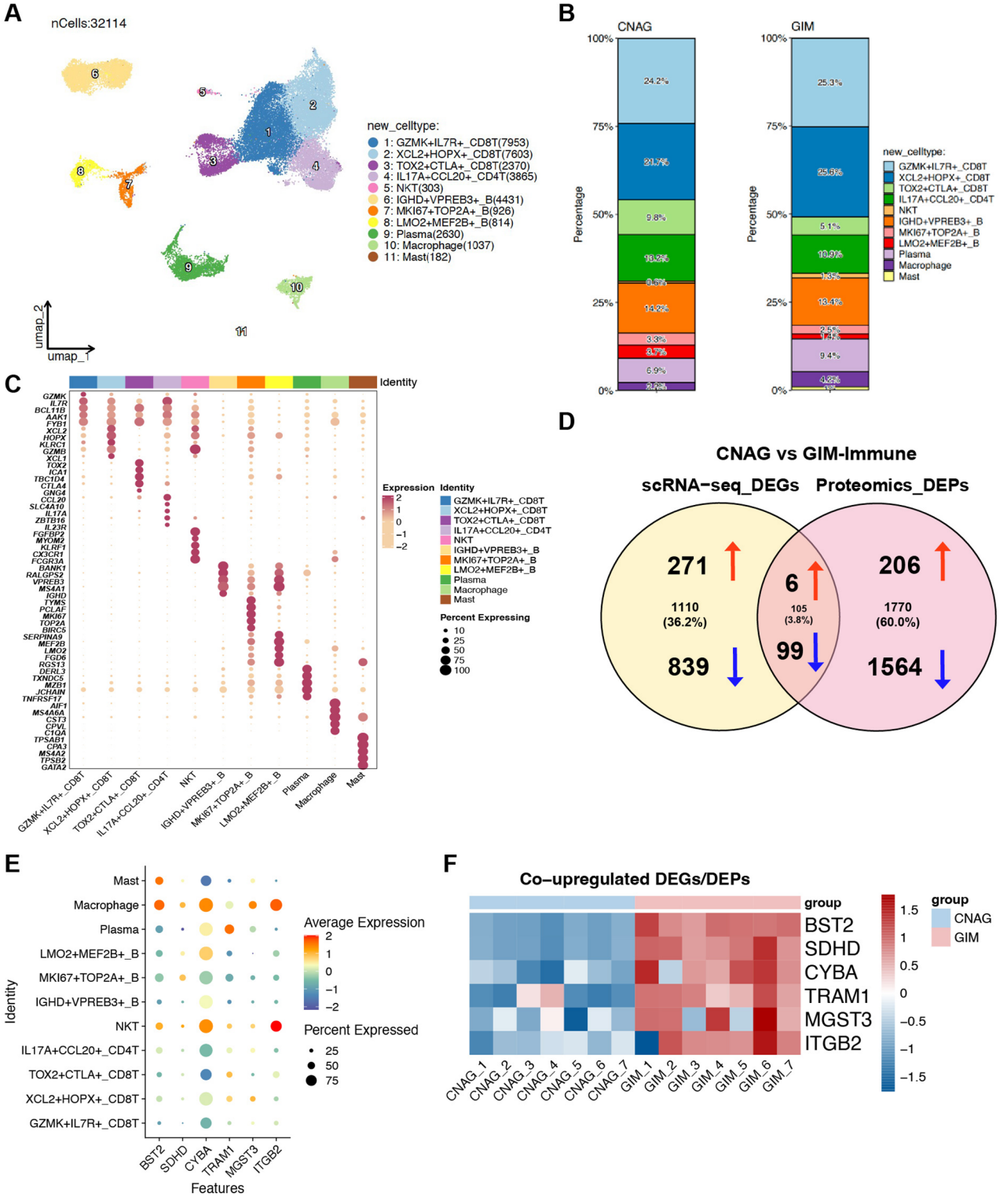

Fig. 7 Immune cell-associated differential protein profiles in GIM revealed by integrated scRNA-seq and proteomics. (**A**) UMAP visualization of immune cell subpopulations. (**B**) Bar plot showing the proportional abundance of immune cell subclusters in CNAG and GIM tissues. (**C**) Dot plot displaying the top 5 marker gens for each immune cell subpopulation. (**D**) Venn diagram identifying the overlapping DEGs from scRNA-seq data and DEPs from proteomic analysis within immune cells. (**E**) Dot plot showing the expression patterns of the commonly upregulated DEGs/DEPs across different immune cell subtypes. (**F**) Heatmap depicting the expression levels of six commonly upregulated DEPs in individual tissue samples from the CNAG and GIM groups, based on proteomic data

with intercellular adherens junctions. This finding suggests that these proteins play a pivotal role in maintaining the structural integrity and function of the gastric epithelium [44]. Alterations in these junctions demonstrate disrupted gastric mucosal barrier integrity during GIM progression, which not only enhances epithelial cell motility but also facilitates penetration of pathogens, toxins, and inflammatory mediators across the epithelial layer, which may initiate inflammatory responses or exacerbate pre-existing inflammation [45].

Our integrated single-cell transcriptomic and proteomic analysis revealed that NEDD8 was significantly upregulated in the epithelial cells of GIM compared to CNAG. As a ubiquitin-like protein, NEDD8 regulates various developmental biological processes through a post-translational modification known as neddylation [29]. The Cullin protein family represents the major neddylation substrate. Neddylated Cullins activate Cullin-RING E3 ubiquitin ligases (CRLs), which orchestrate ubiquitination and degradation of approximately 20% cellular proteins, governing cell cycle progression, differentiation, apoptosis, and embryogenesis [46]. The neddylation pathway is frequently overactivated in various malignancies and is closely associated with tumor cell proliferation, migration, and chemoresistance [47, 48]. For instance, the overexpression of NEDD8 in esophageal squamous cell carcinoma has been identified as a potential therapeutic target [49]. Due to the critical role of this pathway in cancer, inhibitors targeting the NEDD8-activating enzyme (NAE), such as MLN4924, have been developed and have demonstrated significant antitumor activity [50]. It has been shown to enhance the activity of NK cells against multiple myeloma cells [51]. Critically, more than providing a molecular atlas, our discovery of the NEDD8 pathway's specific upregulation in *H. pylori*-associated GIM presents a potential therapeutic window for premalignant interception. Given that NAE inhibitors are already undergoing clinical evaluation in oncology, our findings provide a rationale for exploring their potential as chemopreventive agents. Specifically, targeting the neddylation-NF-κB axis might modulate the hyperproliferative state of the metaplastic epithelium, thereby potentially mitigating the risk of progression from GIM to gastric adenocarcinoma.

Beyond epithelial reprogramming, our data uncover a coordinated re-patterning of the surrounding stroma and mucosal immune milieu that is likely to license, rather than merely accompany, the emergence of GIM. Specifically, we observed profound degradation of extracellular matrix (ECM) integrity, characterized by downregulation of structural genes (COL5A2, POSTN, MXRA5) and depletion of Fibro_C1/C2 fibroblast subsets critical for ECM maintenance. In healthy tissue, the ECM provides a restrictive scaffold that maintains epithelial polarity and differentiation [52]. The loss of key structural proteins like Periostin and Collagen V implies a disorganized tissue remodeling process, potentially facilitating the cellular motility and plasticity required for the metaplastic shift from a gastric to an intestinal phenotype [53]. Concurrently, our integrated analyses revealed 6 concordantly upregulated in the immune compartment. The upregulation of CYBA, a critical component of the NADPH oxidase complex, indicates increased production of ROS by macrophages [54]. Similarly, BST2 is known to amplify anti-viral and pro-inflammatory signaling [55, 56]. This oxidative and inflammatory stress creates a "mutagenic field", forcing gastric epithelial cells to adapt by dedifferentiating or transdifferentiating into metaplastic cells as a survival mechanism. The high expression of ITGB2 can influence the onset and progression of GC development via the CXCL1-CXCR2 axis [57].

Despite the comprehensive nature of this multi-omics atlas, several limitations warrant consideration. First, the inherent difficulty of obtaining human gastric tissues via endoscopy limited our sample size for proteomic analysis. Second, single-cell dissociation inevitably results in loss of spatial context. Future studies leveraging spatial transcriptomics will be essential to delineate precise cellular heterogeneity and spatial distribution patterns within metaplasia lesions. Finally, while we performed functional validation of NEDD8 as a significantly upregulated molecule in GIM, the underlying molecular mechanisms remain to be fully elucidated.

Conclusion

In summary, we have constructed a high-resolution molecular landscape of GIM by integrating proteomic profiling with single-cell transcriptomics. This dataset serves as a high-value resource, offering an unprecedented map of the molecular landscape across the metaplastic transition. Our study highlights the profound remodeling of the immune microenvironment and identifies the NEDD8 pathway as a critical, *H. pylori*-responsive node in epithelial reprogramming. Furthermore, our functional assays using MLN4924 demonstrate that inhibiting the neddylation pathway can attenuate the pro-inflammatory and hyperproliferative responses in gastric cells, providing a mechanistic link between this pathway and GIM dynamics. Collectively, these findings not only clarify the molecular heterogeneity of GIM but also provide a foundational resource for the development of targeted diagnostic tools and therapeutic strategies aimed at intercepting gastric carcinogenesis at its premalignant stage.

Supplementary Information

The online version contains supplementary material available at https://doi.org/10.1186/s12967-026-08150-w.

Supplementary Material 1: Figure S1, supplementary to Figure 1. (A, B) Dot plot (A) and UMAP plot (B) showing the specific markers used for the identification of each cell type. (C) UMAP plot illustrating cellular heterogeneity across the CNAG and GIM stages. (D) Heatmaps from CellChat analysis displaying the number and strength of cellular interacting signaling pathways in GIM lesions compared with CNAG. (E) Circle plots depicting the number of intercellular signaling pathways among distinct cell types in CNAG and GIM lesions

Supplementary Material 2: Figure S2, supplementary to Figure 3. (A-C) UMAP plots showing the expression patterns of (A) MMP9, (B) CTSG and (C) LTF across distinct cell types in CNAG and GIM lesions (left), along with the differential protein expression of these molecules between the two groups revealed by proteomic analysis

Supplementary Material 3: Figure S3, supplementary to Figure 4. (A) UMAP plot showing the unsupervised clustering of epithelial cell subsets into 15 distinct clusters following dimensionality reduction. (B) UMAP plot further illustrating the cellular heterogeneity of epithelial cell subsets across the CNAG and GIM stage. (C) Monocle 3 analysis revealing the dynamic expression changes of APOA4, HLA-DPB1 and OLFM4 genes along the developmental trajectory. (D) Violin plots displaying the expression patterns of the indicated genes across distinct gastric epithelial cell subsets

Supplementary Material 4: Figure S4, supplementary to Figure 5. (A) Dot plot displaying epithelial cell-specific genes among downregulated DEGs/DEPs. (B) Violin and box plots showing NEDD8 expression levels in human CNAG and GIM tissues. (C, E) AGS (C) and HFE145 (E) cells were transfected with NEDD8 siRNA. qRT-PCR was performed to confirm the knockdown efficiency of NEDD8. (D–F) After the knockdown of NEDD8 and H. pylori treatment, the expression of CXCL1, IL-1β, IL-6, and IL-8 was measured by qRT-PCR. *P＜0.05, **P＜0.01, ***P＜0.001

Supplementary Material 5: Figure S5. Supplementary to Figures 6 and 7. (A) UMAP plot showing the expression of marker genes for endothelial cells (PECAM1, CDH5), fibroblasts (PDGFRA, COL1A1) and smooth muscle cells (TAGLN, ACTA2), confirming the accuracy of cell type identification. (B) GO enrichment analysis of proteins downregulated in immune cells from GIM lesions

Supplementary Material 6

Supplementary Material 7

Supplementary Material 8

Supplementary Material 9

Supplementary Material 10

Acknowledgements
This work was supported by the Key Laboratory Project of Digestive Diseases in Jiangxi Province (2024SSY06101), and Jiangxi Clinical Research Center for Gastroenterology (20223BCG74011). We thank the OE biotech (Shanghai) for their technical support in proteomic sequencing.

Author contributions
Conceptualization: N. Li, and HJ. Ke; Methodology: N. Li, YM. Ye, XM. Gong, and SJ. Liu; Tissue samples collection: N. Hu, HJ. Zhang, X. Fei, ZP. Chen and AF. Huang; bioinformatic analysis: YM. Ye; Experiments: XM. Gong, YM. Ye and WT. Fan, AF. Huang; Statistical analysis: XM. Gong; Histopathology: XX. He, Y. Hu; Writing-original Draft: N. Li, HJ. Ke and YM. Ye; Writing-Review& Editing: N. Li, HJ. Ke, YM. Ye and H. Wang, and Y. Zhu; Supervision: N. Li, HJ. Ke, NH. Lu and Y. Zhu; Funding Acquisition: N. Li, Y. Zhu and H. Wang; Supervision: N. Li, Y. Zhu.

Funding
This work was supported by the National Natural Science Foundation of China (82260119, 82170580, and 82400657), the National Science and Technology Major Project of China (No. 2025ZD0545302), the Natural Science Foundation of Jiangxi Province (20242BAB26117, and 20242BAB25436), Jiangxi Provincial Health Technology Project (202410013 and 202410174), and the Clinical Research and Cultivation Project of the First Affiliated Hospital of Nanchang University (No. YFYLCYJPY2025070).

Data availability
The single-cell RNA sequencing data were sourced from two publicly available GEO datasets: GSE249874, which was generated in our previously published study, and GSE134520, an independent single-cell sequencing dataset. The proteomic profile data in this study have been deposited to ProteomeXchange Consortium (https://www.proteomexchange.org/) via the iProX partner repository with the dataset identifier PXD071234.

Declarations

Ethics approval and consent to participate
This work was approved by the Ethics Committee of the First Affiliated Hospital of Nanchang University under protocol number (2023) CDYFYYLK (01–009). The informed consent was obtained from all participants involved in the study. All procedures were carried out in accordance with the principles of the Declaration of Helsinki.

Competing interests
The authors declare no competing interests.

Received: 16 January 2026 / Accepted: 12 April 2026
Published online: 20 April 2026

References

1. Bray F, Laversanne M, Sung H, Ferlay J, Siegel RL, Soerjomataram I, Jemal A. Global cancer statistics 2022: GLOBOCAN estimates of incidence and mortality worldwide for 36 cancers in 185 countries. CA Cancer J Clin. 2024;74:229–63.
2. Thrift AP, Wenker TN, El-Serag HB. Global burden of gastric cancer: epidemiological trends, risk factors, screening and prevention. Nat Rev Clin Oncol. 2023;20:338–49.
3. Guan WL, He Y, Xu RH. Gastric cancer treatment: recent progress and future perspectives. J Hematol Oncol. 2023;16:57.
4. Smyth EC, Nilsson M, Grabsch HI, van Grieken NC, Lordick F. Gastric cancer. Lancet. 2020;396:635–48.
5. Malfertheiner P, Camargo MC, El-Omar E, Liou JM, Peek R, Schulz C, Smith SI, Suerbaum S. Helicobacter pylori infection. Nat Rev Dis Primers. 2023;9:19.
6. Wizenty J, Sigal M. Helicobacter pylori, microbiota and gastric cancer - principles of microorganism-driven carcinogenesis. Nat Rev Gastroenterol Hepatol. 2025.
7. Sugano K, Moss SF, Kuipers EJ. Gastric Intestinal Metaplasia: Real Culprit or Innocent Bystander as a Precancerous Condition for Gastric Cancer? Gastroenterology. 2023;165:1352–66. e1351.
8. Huang KK, Ma H, Chong RHH, Uchihara T, Lian BSX, Zhu F, Sheng T, Srivastava S, Tay ST, Sundar R, et al. Spatiotemporal genomic profiling of intestinal metaplasia reveals clonal dynamics of gastric cancer progression. Cancer Cell. 2023;41:2019–2037.e2018.
9. Chen YC, Malfertheiner P, Yu HT, Kuo CL, Chang YY, Meng FT, Wu YX, Hsiao JL, Chen MJ, Lin KP, et al. Global Prevalence of Helicobacter pylori Infection and Incidence of Gastric Cancer Between 1980 and 2022. Gastroenterology. 2024;166:605–19.
10. Modi N, Chen Y, Dong X, Hu X, Lau GW, Wilson KT, Peek RM Jr., Chen LF. BRD4 Regulates Glycolysis-Dependent Nos2 Expression in Macrophages Upon H pylori Infection. Cell Mol Gastroenterol Hepatol. 2024;17:292–e308291.
11. Fei X, Li N, Xu X, Zhu Y. Macrophage biology in the pathogenesis of helicobacter pylori infection. Crit Rev Microbiol. 2024:1–18.
12. Wang H, Xu X, Ouyang Y, Fei X, He C, Yang X, Ren Y, Zhou Y, Chen S, Hu Y, et al. The Protective Role of DDIT4 in Helicobacter pylori-induced Gastric Metaplasia Through Metabolic Regulation of Ferroptosis. Cell Mol Gastroenterol Hepatol. 2025;19:101448.
13. Xu X, Fei X, Wang H, Wu X, Zhan Y, Li X, Zhou Y, Shu C, He C, Hu Y, et al. Helicobacter pylori infection induces DNA double-strand breaks through the ACVR1/IRF3/POLD1 signaling axis to drive gastric tumorigenesis. Gut Microbes. 2025;17:2463581.
14. Imai S, Ooki T, Murata-Kamiya N, Komura D, Tahmina K, Wu W, Takahashi-Kanemitsu A, Knight CT, Kunita A, Suzuki N, et al. Helicobacter pylori CagA elicits BRCAness to induce genome instability that may underlie bacterial gastric carcinogenesis. Cell Host Microbe. 2021;29:941–e958910.

15. Li N, Xu X, Yang H, Wang H, Ouyang Y, Zhou Y, Peng C, Yuan Z, He C, Zeng C, Hong J. Activation of Aquaporin 5 by carcinogenic Helicobacter pylori infection promotes epithelial-mesenchymal transition via the MEK/ERK pathway. Helicobacter. 2021;26:e12842.
16. Goldenring JR, Mills JC. Cellular Plasticity, Reprogramming, and Regeneration: Metaplasia in the Stomach and Beyond. Gastroenterology. 2022;162:415–30.
17. Jeong H, Lee B, Kim KH, Cho SY, Cho Y, Park J, Lee Y, Oh Y, Hwang BR, Jang AR, et al. WFDC2 Promotes Spasmolytic Polypeptide-Expressing Metaplasia Through the Up-Regulation of IL33 in Response to Injury. Gastroenterology. 2021;161:953–e967915.
18. Hayakawa Y, Ariyama H, Stancikova J, Sakitani K, Asfaha S, Renz BW, Dubeykovskaya ZA, Shibata W, Wang H, Westphalen CB, et al. Mist1 Expressing Gastric Stem Cells Maintain the Normal and Neoplastic Gastric Epithelium and Are Supported by a Perivascular Stem Cell Niche. Cancer Cell. 2015;28:800–14.
19. Wang H, Liu S, Fei X, Fan W, Ye Y, Xu X, Chen Z, Gong X, Zhou Y, Wu X, et al. Lipidomics and single-cell transcriptomics uncover aberrant lipid metabolism in metaplasia lesions during gastric carcinogenesis. J Gastroenterol. 2025.
20. Li N, Chen S, Xu X, Wang H, Zheng P, Fei X, Ke H, Lei Y, Zhou Y, Yang X, et al. Single-cell transcriptomic profiling uncovers cellular complexity and microenvironment in gastric tumorigenesis associated with Helicobacter pylori. J Adv Res. 2025;74:471–91.
21. Huang KK, Ramnarayanan K, Zhu F, Srivastava S, Xu C, Tan ALK, Lee M, Tay S, Das K, Xing M, et al. Genomic and Epigenomic Profiling of High-Risk Intestinal Metaplasia Reveals Molecular Determinants of Progression to Gastric Cancer. Cancer Cell. 2018;33:137–e150135.
22. Takeuchi C, Yamashita S, Liu YY, Takeshima H, Sasaki A, Fukuda M, Hashimoto T, Naka T, Ishizu K, Sekine S, et al. Precancerous nature of intestinal metaplasia with increased chance of conversion and accelerated DNA methylation. Gut. 2024;73:255–67.
23. Wang K, Yuen ST, Xu J, Lee SP, Yan HH, Shi ST, Siu HC, Deng S, Chu KM, Law S, et al. Whole-genome sequencing and comprehensive molecular profiling identify new driver mutations in gastric cancer. Nat Genet. 2014;46:573–82.
24. Mun DG, Bhin J, Kim S, Kim H, Jung JH, Jung Y, Jang YE, Park JM, Kim H, Jung Y, et al. Proteogenomic Characterization of Human Early-Onset Gastric Cancer. Cancer Cell. 2019;35:111–e124110.
25. Ma J, Chen T, Wu S, Yang C, Bai M, Shu K, Li K, Zhang G, Jin Z, He F, et al. iProX: an integrated proteome resource. Nucleic Acids Res. 2019;47:D1211–7.
26. Chen T, Ma J, Liu Y, Chen Z, Xiao N, Lu Y, Fu Y, Yang C, Li M, Wu S, et al. iProX in 2021: connecting proteomics data sharing with big data. Nucleic Acids Res. 2022;50:D1522–7.
27. Szklarczyk D, Gable AL, Lyon D, Junge A, Wyder S, Huerta-Cepas J, Simonovic M, Doncheva NT, Morris JH, Bork P, et al. STRING v11: protein-protein association networks with increased coverage, supporting functional discovery in genome-wide experimental datasets. Nucleic Acids Res. 2019;47:D607–13.
28. Yue SSK, Tong Y, Siu HC, Ho SL, Law SYK, Tsui WY, Chan D, Huang Y, Chan ASY, Yun SW, et al. Divergent lineage trajectories and genetic landscapes in human gastric intestinal metaplasia organoids associated with early neoplastic progression. Gut. 2025;74:522–38.
29. Baek K, Krist DT, Prabu JR, Hill S, Klügel M, Neumaier LM, von Gronau S, Kleiger G, Schulman BA. NEDD8 nucleates a multivalent cullin-RING-UBE2D ubiquitin ligation assembly. Nature. 2020;578:461–6.
30. Mathewson N, Toubai T, Kapeles S, Sun Y, Oravecz-Wilson K, Tamaki H, Wang Y, Hou G, Sun Y, Reddy P. Neddylation plays an important role in the regulation of murine and human dendritic cell function. Blood. 2013;122:2062–73.
31. Xirodimas DP, Saville MK, Bourdon JC, Hay RT, Lane DP. Mdm2-mediated NEDD8 conjugation of p53 inhibits its transcriptional activity. Cell. 2004;118:83–97.
32. Dinis-Ribeiro M, Shah S, El-Serag H, Banks M, Uedo N, Tajiri H, Coelho LG, Libanio D, Lahner E, Rollan A, et al. The road to a world-unified approach to the management of patients with gastric intestinal metaplasia: a review of current guidelines. Gut. 2024;73:1607–17.
33. Totoki Y, Saito-Adachi M, Shiraishi Y, Komura D, Nakamura H, Suzuki A, Tatsuno K, Rokutan H, Hama N, Yamamoto S, et al. Multiancestry genomic and transcriptomic analysis of gastric cancer. Nat Genet. 2023;55:581–94.
34. Yasuda T, Wang YA. Gastric cancer immunosuppressive microenvironment heterogeneity: implications for therapy development. Trends Cancer. 2024;10:627–42.
35. Harding HP, Zhang Y, Zeng H, Novoa I, Lu PD, Calfon M, Sadri N, Yun C, Popko B, Paules R, et al. An integrated stress response regulates amino acid metabolism and resistance to oxidative stress. Mol Cell. 2003;11:619–33.
36. Correa P. Human gastric carcinogenesis: a multistep and multifactorial process–First American Cancer Society Award Lecture on Cancer Epidemiology and Prevention. Cancer Res. 1992;52:6735–40.
37. Brown JW, Cho CJ, Mills JC. Paligenosis: Cellular Remodeling During Tissue Repair. Annu Rev Physiol. 2022;84:461–83.
38. Biamonti G, Caceres JF. Cellular stress and RNA splicing. Trends Biochem Sci. 2009;34:146–53.
39. Braunschweig U, Gueroussov S, Plocik AM, Graveley BR, Blencowe BJ. Dynamic integration of splicing within gene regulatory pathways. Cell. 2013;152:1252–69.
40. Lee SH, Contreras Panta EW, Gibbs D, Won Y, Min J, Zhang C, Roland JT, Hong SH, Sohn Y, Krystofiak E, et al. Apposition of Fibroblasts With Metaplastic Gastric Cells Promotes Dysplastic Transition. Gastroenterology. 2023;165:374–90.
41. Zhang M, Hu S, Min M, Ni Y, Lu Z, Sun X, Wu J, Liu B, Ying X, Liu Y. Dissecting transcriptional heterogeneity in primary gastric adenocarcinoma by single cell RNA sequencing. Gut. 2021;70:464–75.
42. Wang R, Song S, Qin J, Yoshimura K, Peng F, Chu Y, Li Y, Fan Y, Jin J, Dang M, et al. Evolution of immune and stromal cell states and ecotypes during gastric adenocarcinoma progression. Cancer Cell. 2023;41:1407–e14261409.
43. Wei H, Li W, Zeng L, Ding N, Li K, Yu H, Jiang F, Yin H, Xia Y, Deng C, et al. OLFM4 promotes the progression of intestinal metaplasia through activation of the MYH9/GSK3β/β-catenin pathway. Mol Cancer. 2024;23:124.
44. Horowitz A, Chanez-Paredes SD, Haest X, Turner JR. Paracellular permeability and tight junction regulation in gut health and disease. Nat Rev Gastroenterol Hepatol. 2023;20:417–32.
45. Jeong HJ, Park JH, Kang JH, Sabate Del Rio J, Kong SH, Park TE. Organoid-Based Human Stomach Micro-Physiological System to Recapitulate the Dynamic Mucosal Defense Mechanism. Adv Sci (Weinh). 2023;10:e2300164.
46. Zhou L, Jiang Y, Luo Q, Li L, Jia L. Neddylation: a novel modulator of the tumor microenvironment. Mol Cancer. 2019;18:77.
47. Song Q, Feng S, Peng W, Li A, Ma T, Yu B, Liu HM. Cullin-RING Ligases as Promising Targets for Gastric Carcinoma Treatment. Pharmacol Res. 2021;170:105493.
48. Zhou Q, Lin W, Wang C, Sun F, Ju S, Chen Q, Wang Y, Chen Y, Li H, Wang L, et al. Neddylation inhibition induces glutamine uptake and metabolism by targeting CRL3(SPOP) E3 ligase in cancer cells. Nat Commun. 2022;13:3034.
49. Xian J, Wang S, Jiang Y, Li L, Cai L, Chen P, Liu Y, Zeng X, Chen G, Ding C, et al. Overexpressed NEDD8 as a potential therapeutic target in esophageal squamous cell carcinoma. Cancer Biol Med. 2021;19:504–17.
50. Soucy TA, Smith PG, Milhollen MA, Berger AJ, Gavin JM, Adhikari S, Brownell JE, Burke KE, Cardin DP, Critchley S, et al. An inhibitor of NEDD8-activating enzyme as a new approach to treat cancer. Nature. 2009;458:732–6.
51. Petillo S, Sproviero E, Loconte L, Cuollo L, Zingoni A, Molfetta R, Fionda C, Soriani A, Cerboni C, Petrucci MT, et al. NEDD8-activating enzyme inhibition potentiates the anti-myeloma activity of natural killer cells. Cell Death Dis. 2023;14:438.
52. Naba A. Mechanisms of assembly and remodelling of the extracellular matrix. Nat Rev Mol Cell Biol. 2024;25:865–85.
53. Wu Y, Li S, Yu H, Zhang S, Yan L, Guan X, Xu W, Wang Z, Lv A, Tian X, et al. Integrative Single-Cell and Spatial Transcriptomics Analysis Reveals ECM-remodeling Cancer-associated Fibroblast-Derived POSTN as a Key Mediator in Pancreatic Ductal Adenocarcinoma Progression. Int J Biol Sci. 2025;21:3573–96.
54. San José G, Fortuño A, Beloqui O, Díez J, Zalba G. NADPH oxidase CYBA polymorphisms, oxidative stress and cardiovascular diseases. Clin Sci (Lond). 2008;114:173–82.
55. Olety B, Peters P, Wu Y, Usami Y, Göttlinger H. HIV-1 propagation is highly dependent on basal levels of the restriction factor BST2. Sci Adv. 2021;7:eabj7398.
56. Kong N, Shan T, Wang H, Jiao Y, Zuo Y, Li L, Tong W, Yu L, Jiang Y, Zhou Y, et al. BST2 suppresses porcine epidemic diarrhea virus replication by targeting and degrading virus nucleocapsid protein with selective autophagy. Autophagy. 2020;16:1737–52.
57. Shang C, Zhang Y, Wang Y, Zhao W, Sun X, Dong X, Qiao H. Role of ITGB2 protein structure and molecular mechanism in precancerous lesions of gastric cancer: Influencing the occurrence and development of cancer through the CXCL1-CXCR2 axis. Int J Biol Macromol. 2025;296:139772.

Publisher's note